Evidence for Melt Leakage from the Hawaiian Plume above the Mantle Transition Zone

Saswata Hier-Majumder[a,b], Maxim D. Ballmer[c,d], Matthew Agius[e], Catherine Rychert[e], Nicholas Harmon[e]

[a]*Department of Earth Sciences, Royal Holloway University of London, Egham, Surrey, TW20 0EX, UK.*
[b]*AAAS Science and Technology Policy Fellow, Advanced Scientific Computing and Research, Office of Science, Department of Energy, Germantown, MD, USA.*
[c]*ETH Zürich, Switzerland*
[d]*University College London, UK*
[e]*University of Southampton, UK*

Abstract

Dehydration reactions at the top of the mantle transition zone (MTZ) can stabilize partial melt in a seismic low-velocity layer (LVL), but the seismic effects of temperature, melt and volatile content are difficult to distinguish. We invert P-to-S receiver function phases converted at the top and bottom of a LVL above the MTZ beneath Hawaii. To separate the thermal and melting related seismic anomalies, we carry out over 10 million rock physics inversions. These inversions account for variations arising from the Clapeyron slope of phase transition, bulk solid composition, dihedral angle, and mantle potential temperature. We use two independent seismic constraints to evaluate the temperature and shear wave speed within the LVL. The thermal anomalies reveal the presence of a hot and seismically slow plume stem surrounded by a "halo" of cold and fast mantle material. In contrast to this

Email address: `Saswata.Hier-Majumder@rhul.ac.uk` (Saswata Hier-Majumder)

temperature distribution, the plume stem contains less than 0.5 vol% melt, while the surrounding LVL contains up to 1.7 vol% melt, indicating lateral transport of the melt. The temperature within the LVL, calculated from seismic observations of MTZ thickness, suggests that the observed small degrees of melting are sustained by the presence of volatiles such as CO_2 and H_2O. We estimate the Hawaiian plume loses up to 1.9 Mt/yr H_2O and 10.7 Mt/yr CO_2 to the LVL, providing a crucial missing flux for global volatile cycles.
Keywords: Mantle Plume, Transition Zone, LVL, Volatiles, Melting

---

1. Introduction

Mantle plumes are major pathways for heat (Ballmer et al., 2013) and volatile (Burton et al., 2013; Dasgupta and Hirschmann, 2010; Kelemen and Manning, 2015; Plank and Manning, 2019) transfer from the lower mantle to the surface of the Earth. The interaction between ascending plumes and the surrounding mantle can have significant implications for global volatile cycles. Drastic reduction in the water storage capacity between minerals within and above the mantle transition zone (MTZ) (Kohlstedt et al., 1996) can lead to dehydration melting within the ascending plume (Bercovici and Karato, 2003; Ohtani et al., 2004). Sharp reduction in the melting temperature of carbonated basalts just above the MTZ (Thomson et al., 2016) can also trigger decarbonation melting of recycled oceanic crust components in the plume material atop the MTZ. A partially molten region above the MTZ may provide a reservoir for incompatible elements and volatiles, as they preferentially partition into melts (Aubaud, 2004; Hirschmann and Dasgupta, 2009). The seismically anomalous low velocity layer (LVL)—characterized by 2–3% reduction in shear wave speed (Agius et al., 2017; Hier-Majumder and Courtier, 2011; Hier-Majumder et al., 2014; Tauzin et al., 2010; Vinnik and Farra, 2007) and small amounts ($\sim$1 vol%) of partial melt (Hier-Majumder and Courtier, 2011; Hier-Majumder et al., 2014)—is one such possible reservoir. Among the several tectonic settings in which LVLs are observed (Tauzin et al., 2010; Vinnik and Farra, 2007), their potential role in storing mantle volatiles near subduction zones has been discussed (Hier-majumder and Tauzin, 2017; Sun et al., 2020), but volatile fluxes to the LVLs associated with plumes remains relatively poorly quantified (Dasgupta and Hirschmann, 2010).

Sequestration of partial melt from the plume into the LVL can impede the volatile transport to the Hawaiian volcanoes from the lower mantle. The high volatile content of the Hawaiian plume, evidenced by 2.4 Mt/yr CO_2 emissions from Kilauea volcano (Burton et al., 2013), is derived from recycled oceanic crust (Sobolev et al., 2007), which contains up to 450 ppm H_2O (Bizimis and Peslier, 2015) and 250 ppm CO_2 (Anderson and Poland, 2017). Volatile-rich melt generation in the LVL and subsequent interaction between these melts and the plume is indicated by geochemical signatures with mixing trends between multiple reservoirs (Hauri, 2002). Despite this geochemical evidence, geophysical observations of melt loss from the plume and quantification of associated volatile fluxes remained elusive.

While heat and mass transfer by mantle plumes to the upper mantle is thought to be interrupted by volatile-rich melt pooling above the mantle transition zone (MTZ) (Bercovici and Karato, 2003), quantifying the magnitudes of melt and dissolved volatile fluxes from seismic anomalies remain challenging, as both elevated temperature and melt have similar seismic signatures

(Tauzin et al., 2010; Vinnik and Farra, 2007; Wei and Shearer, 2017; Wolfe et al., 2009, 2011). Previous seismic and rock physics studies of plume-related LVLs either focused on mapping anomalous seismic wave speeds in the LVL (Laske et al., 2009; Tauzin et al., 2010; Vinnik and Farra, 2007) or calculating an average melt fraction (Hier-Majumder et al., 2014). Distinction between the spatial variations due to temperature and melt content has remained difficult, as both sustain low seismic wave speeds. In this work, we overcome this limitation by carrying out a detailed analysis of teleseismic P-to-S phase conversions obtained from permanent and temporary land and ocean bottom broadband seismometers from the "Plume-lithosphere undersea melt experiment" (PLUME) (Agius et al., 2017; Laske et al., 2009), quantifying the distribution of both temperature and melt in the LVL beneath Hawaii. Both the high lateral resolution of the previous receiver function work (Agius et al., 2017) combined with our formal accounting of error in the inversions allow us to map the distribution of both temperature and melt in the LVL beneath Hawaii with unprecedented resolution. While a previous study by Hier-Majumder et al. (2014) estimated $\sim$1 vol% melting in the Hawaiian LVL, the limited lateral resolution of seismic data in this work was insufficient to map the lateral distribution of melt.

In the following section, we present a detailed discussion of the methods of seismic and rock physics analysis, a description of the parameter space, and the method of uncertainty calculation arising from uncertainties in the rock physics inversion. Section 3 outlines the results of the rock physics inversion, including a detailed description of the effect of each parameter on the calculated melt volume fraction. Based on our results, we present a hypothesis on plume leakage and its impact on the global volatile cycles in Section 4. Finally, we outline the key findings of this work in Section 5. We also derive a zeroth-order equation for volatile flux associated with melt leakage in Appendix A.

2. Methods

2.1. Receiver functions

The dataset exploited here is acquired from the previous study of Agius et al. (2017). For this dataset, teleseismic P-to-S phase conversions were obtained from permanent and temporary land and ocean bottom broadband seismometers located across the Hawaiian archipelago (*e.g.* Hawaiian Plume-Lithosphere Undersea Mantle Experiment–PLUME (Laske et al., 2009, 2011)). The seismic model extends outside the region shown, for instance >24 degrees North (Agius et al., 2017). We only present the robust regions for the purposes of this work, thus avoiding artefacts owing to areas of lower resolution. Preprocessing of the waveforms for ocean stations included removal of the tilt noise on the vertical components (Crawford and Webb, 2000), removal of the compliance noise (Bell et al., 2015), and reorientation of the horizontal components. Both land and ocean stations were then band-pass filtered between 0.05–0.2 Hz and had the horizontal components rotated to the radial and transverse components. Waveforms of teleseismic earthquakes with a magnitude greater than $M_w = 5.5$ and with an epicentral distance to the stations between 35° and 80° were extracted for further analysis. Manually selected P phases were deconvolved from the radial component using the extended multitaper frequency domain deconvolution technique

(Rychert et al., 2013) to produce a receiver function. A positive amplitude receiver function phase indicates a wave speed increase with depth, whereas a negative amplitude indicates a wave speed decrease.

Each receiver function was migrated to depth, and corrected for the sphericity of the Earth, thus diminishing edge effects. A one-dimensional, crust-corrected reference model (PREM, (Dziewonski and Anderson, 1981; Leahy et al., 2010), Crust 1.0 (Laske et al., 2013)) was applied with additional corrections for the stations' elevations (Figure 1). As an example of absence of edge effects, Figure 1 shows the 410 km discontinuity 'rises' and 'deepens' again towards the edge. Estimates for the uncertainties of the receiver functions were determined with bootstrap resampling and averaging of the receiver function traces within a bin. The migrated receiver functions were then back-projected along the theoretical ray path and stacked onto a three-dimensional (3-D) grid with a lateral spacing of 1^o by 1^o and a 1 km depth vertical spacing. The grid is smoothed with a radius corresponding to the Fresnel zone of the waveform (Figure 1). The depth and amplitude of the positive peak close to the 410 and 660 km depth were selected as the mantle transition zone discontinuities. Similarly, the depth and amplitude of the negative peak atop the 410 were selected specifically for this study. Sporadic positive polarity phases in the 200-350 km depth range in the model of Agius et al. (2017), are likely related to small scale heterogeneity, as has frequently been observed and described by other authors (*e.g.* Deuss, 2009). We also observe phases within the transition zone similar to detections reported by previous studies (Shearer, 1990). The standard error of the amplitudes and of the discontinuity depths are shown in the supplementary material.

Based on this analysis of the dataset, we attempt to determine lateral variations in the presence or absence of melt across the region. Such determination becomes achievable with our 3-D receiver function migration approach using a wide aperture array (Agius et al., 2017). Also note that our inversion scheme fully accounts for and propagates errors quantitatively. Although near-plume melt imaging is seemingly inconsistent with one previous receiver function study that found no evidence for a melt layer above the 410 near plumes, the scale of our observation would not likely be resolvable by the single station stack approach of the previous study (Tauzin et al., 2010). We previously verified the robustness of interpreted transition-zone thickness variations by implementing a variety of migrations models (Agius et al., 2017). These models involve 1-D (PREM), 3-D with a central low shear wave speed plume, and 3-D with a plume surrounded by fast shear wave speeds, after anomaly magnitudes reported by Wolfe et al. (2009). These tests showed that the observed variability in transition zone thickness are robust.

2.2. Rock physics analysis

We carried out rock physics analysis using the numerical code MuMaP (version 2.1, Hier-Majumder, 2020; Hier-Majumder et al., 2014). In this method, we use two independent sets of seismic observations to constrain the temperature and shear wave speed at each location. We then use the mineral physics model of Xu et al. (2008) in combination with the calculated temperature to isolate the effect of the bulk composition and temperature on the seismic signature. Any residual negative anomalies are then attributed to melting. In the following subsections, we describe these details in sequence. Interested readers can see Hier-Majumder et al. (2014) for a more detailed description of the analysis. Interested readers can access the raw data from rock physics inversions from an open-source database (Hier-Majumder et al., 2019).

2.2.1. Temperature

The first step in our analysis involves calculating the temperature at each of the 1681 locations of the dataset. We used two different methods to estimate this temperature at each location (*i.e.*, in two separate sets of rock physics inversions): (1) the thickness of the MTZ (Hier-majumder and Tauzin, 2017; Tauzin and Ricard, 2014) and (2) the topography of the 410 km discontinuity (Hier-Majumder et al., 2014). On one hand, using the MTZ thickness minimizes errors from unknown wave speed anomalies above 410 km depth, including in the crust, which may influence the seismically-inferred depth of the 410 km (Tauzin and Ricard, 2014). On the other hand, using the MTZ thickness as a proxy for temperature neglects any potential radial temperature gradients across the MTZ.

To quantify the uncertainties arising from temperature, we computed the temperature for 9 different Clapeyron slopes of the olivine-wadsleyite transition in the range of 0.5 to 4.5 MPa/K for both sets of measurements. Once the temperature anomalies are calculated, we convert these anomalies to temperature by adding an adiabat with a specified potential temperature and an adiabatic gradient of 0.3 K/km. To test the effects of potential temperature, we carry out inversions for 5 different values of the potential temperature ranging from 1127 to 1527 °C (1400–1800 K).

2.2.2. Bulk solid composition

In addition to temperature, we explore the effects of the excess fraction of eclogite in the LVL mantle, f, on the resultant seismic wave speeds. In our compositional model, the fraction f of the mantle consists of purely basaltic component, while the rest, $1-f$, consists of peridotite. We use the compositional model from Xu et al. (2008), which suggests that the peridotite consists of a mechanical mixture of 18% basalt and 82% harzburgite. The bulk basalt fraction X, the quantity commonly used in the geophysics and mineral-physics literature, and the excess eclogite fraction f, are then related by

$$0.18(1-f)+f=X, \tag{1}$$

where X is expressed as a fraction. In the inversions, we use X to evaluate physical properties according to Xu et al. (2008). In the figures, we use f to indicate the excess fraction of mantle eclogite. According to Sobolev et al. (2007), the plume source material contains approximately 20% eclogite. In the deep eclogitic pool (DEP) atop the transition zone (Ballmer et al., 2013), discussed in Section 4, the solid matrix should be more enriched in eclogite than the plume stem and is expected to have a higher value of f than 0.2. We report the results for a conservative estimate of $f = 0.27$ ($X = 0.4$) for the composition of the LVL matrix. As discussed in Section 3.2 in the region around the plume stem, a higher value of f will lead to a higher predicted median melt volume fraction than our conservative estimate. As a result, our calculated LVL melt fractions remain a conservative estimate.

Once the temperature is evaluated at each point and a bulk solid composition is assigned to the mantle, we proceed to calculate the melt volume fraction from the residual seismic anomaly, described next.

2.2.3. Melting

To calculate melt volume fractions, we start by defining a reference shear wave speed, $V_S^{ref}(X,T)$ and an inferred shear wave speed, V_S^{inf}. The reference shear wave speed is a theoretical value, dependent on the temperature (T) and solid composition (X). Since we calculate the temperature at each point from either the MTZ thickness or the MTZ topography, this value is spatially variable. In contrast, we calculate the inferred shear wave speed from the normalized amplitude, R_{norm}, of the receiver function (Hier-Majumder et al., 2014). As the value of the normalized amplitude is spatially variable, so is V_S^{inf}. Notice, however, this spatial variation is independent of and, as shown later, generally different from the spatial variations in $V_S^{ref}(X,T)$. If, at a location, $V_S^{ref}(X,T) = V_S^{inf}$, no melting is necessary to explain the seismic observation. If, however, these two wave speeds are unequal and $V_S^{ref}(X,T) > V_S^{inf}$, we attribute the anomaly to melting. To quantify the amount of melting from the difference between these two independently derived wave speeds, we define a melt anomaly function, $\xi(\theta,\phi)$, such that

$$V_S^{inf} - \xi(\theta,\phi)V_S^{ref}(X,T) = \epsilon, \tag{2}$$

where $\epsilon \ll 1$ is the residual error of the calculation, θ is the solid-melt dihedral angle, and ϕ is the unknown melt-volume fraction. Using this definition, we can define the residual shear wave speed anomaly as (setting $\epsilon = 0$)

$$\Delta V_S = \frac{V_S^{inf} - V_S^{ref}}{V_S^{ref}} = \xi - 1. \tag{3}$$

Having incorporated the effects of temperature and bulk solid composition in computing V_S^{ref}, ΔV_S is independent from variations in temperature and solid composition within the parameter space of our inversion. Next, we invert the nonlinear, implicit equation (2) to calculate the unknown melt-volume fraction, ϕ, at each location.

2.2.4. Parameter space

To explore the parameter space, we carried out the inversions for 5 different values of mantle potential temperature, 7 dihedral angles between 10^{o} and 40^{o}, 10 different values of X ranging from 0.1 to 0.99, and 9 different values of Clapeyron slope. All these analyses were carried out using 2 different methods to evaluate lateral thermal anomalies in the transition zone (based on either the MTZ thickness, or the topography of the 410-km discontinuity, see above), totaling 6300 analyses for each of the 1681 data locations (or more than 10 million inversions). Using this large parameter space not only allows us to quantify the variations in calculated melt fractions, but also to provide a robust estimate of the uncertainties arising from these variations, discussed in section 2.3.

2.2.5. Calculation of permeability and melt segregation velocity

Once the melt fraction is evaluated at each point, we use the calculated melt volume fraction to obtain the permeability and a zeroth order estimate of melt migration velocity for the given melt fraction. We calculated the permeability of melt from the melt fraction using a microstructural model of melt in tubes at three-grain corners (Turcotte and Schubert, 2001, eq. 9-10). In this model, the permeability, k, is related to the melt fraction, ϕ, by the relation, $k = \left(b^2\phi^2\right)/72\pi$, where we assume $b = 1$ mm is the matrix grain size (Hier-majumder and Tauzin, 2017). To evaluate the melt migration velocity, we use a 1D model of two-phase flow and compaction (Bercovici et al., 2001; Hier-Majumder et al., 2006). In this model, each point is treated as a melting column where the melt segregation from the matrix is governed by compaction within the matrix and density-driven segregation between the melt and the matrix. Following the method outlined by Hier-Majumder and Courtier (2011), we solve the governing partial differential analytically to obtain an expression for the melt segregation velocity as a function of melt volume fraction within the column. For the melt fraction at each location, we use the result of the rock physics inversion. The interested reader is encouraged to see the details of this solution in the work of Hier-Majumder and Courtier (2011).

2.3. Calculation of uncertainties

One of the strengths of our analysis is the identification of the first-order uncertainties and quantification of the error in the calculated melt volume fraction. We do not consider the putative influence of crystal-bound water or melt composition in the reduction of seismic wave speeds. Recent experimental results at LVL-like pressure temperature conditions show that the influence of water on seismic wave speed reduction is small (Schulze et al., 2018). In addition, there is a lack of documented systematic variation of the wave speed in solids as a function of water related point defects in the nominally anhydrous minerals under LVL-like conditions, precluding a parameter space search for uncertainty as carried out in this work. In two previous studies, Hier-Majumder et al. (2014) and Wimert and Hier-Majumder (2012) experimented with the influence of melt composition on the calculations using equations of states of different melts. For small melt volume fractions such as the LVL, the influence of melt composition was found to be insignificantly small. In other words, we only focus on the factors that exert a first-order influence on the calculated wave speed and are sufficiently characterized, thus permitting a systematic parameter-space search.

We calculated the uncertainty in the melt volume fractions, α_ϕ, from the uncertainties (α_i) in the four parameters (η_i): potential temperature (η_T), basalt fraction (η_X), dihedral angle (η_θ), and the Clapeyron slope of olivine-wadsleyite transformation (η_γ). The propagated error is calculated from the uncertainties and gradients $\partial \langle \phi \rangle / \partial \eta_i$, using the formula

$$\alpha_\phi = \sqrt{\sum_i \alpha_i^2 \left(\frac{\partial \langle \phi \rangle}{\partial \eta_i} \right)^2_{j \neq i}} \tag{4}$$

where $\partial \langle \phi \rangle / \partial \eta_i$ is the rate of change of the median melt volume fraction with changes in one of these four parameters, keeping the other three constant. We use uncertainty values of $\alpha_\theta = \pm 5^{\text{o}}$ (Minarik and Watson, 1995), $\alpha_\gamma = \pm 0.8$ MPa/K (Tauzin and Ricard, 2014), and $\alpha_X = \pm 16\%$ (Sobolev et al., 2007) and calculate the derivatives $\partial \langle \phi \rangle / \partial \eta_i$ numerically from our inversions. We evaluate the uncertainty in temperature, α_T, from the standard deviation in the measurement of the MTZ thickness, h_{MTZ}. For a mantle density of ρ, gravity, g, and a Clapeyron slope of γ, we estimate

$$\alpha_T = h_{MTZ} \frac{\rho g}{\gamma}. \tag{5}$$

Using $\rho = 3300$ kg/m^3, $g = 10$ ms^{-2}, $\gamma = 3$ MPa/K, and $h_{MTZ} = 5.8$ km from our data, we get $\alpha_T = 63.8^{\text{o}}$C, which we use in equation (4). Inserting these values in equation (4), we evaluate the error in melt volume fraction $\alpha_\phi = \pm 0.3$ vol%.

3. Results

We carried out two sets of analyses—using two different methods for determining temperature as described in Section 2.2.1—and found that differences between the results are small. For example, the inferred median melt-volume fractions calculated from these two methods differ only by $\sim$0.01 vol%, an order of magnitude smaller than the propagated error. In this section, we report temperatures calculated using our preferred method, MTZ topography, unless stated otherwise.

3.1. Melt distribution within the Hawaiian LVL

The primary seismic observations and a few calculated quantities are mapped in Figure 2. The MTZ beneath Hawaii (Figure 2(a), median thickness 251 km) is characterized by a thin central region surrounded by a thicker, concentric region. While such a feature is absent in the map of LVL thickness in Figure 2(b), the thickest part of the LVL trends SE-NW, being elongated roughly in the direction of plate motion. This correlation between LVL thickness and plate motion suggests that the LVL is possibly a dynamic feature interacting with the ambient mantle flow. We find that the temperature distribution near the 410 km discontinuity displays a bimodal spatial pattern. Consistent with previous seismic P and S-wave tomography models (Wolfe et al., 2009, 2011); the hot and seismically slow plume stem is surrounded by a "halo" of cold and fast material (Figure 2(c)) (Agius et al., 2017).

The separation between the thermal and chemical component of the Hawaiian LVL becomes clear from the map of the inferred and reference seismic wave speeds. As expected, the map of reference wave speed, V_S^{ref},

(Figure 2(d)) closely follows the temperature distribution, with slow wave speeds within the plume stem and fast wave speeds in the cold halo. Such a halo is often interpreted as a curtain of cold downwelling from the base of the lithosphere to the MTZ (Ballmer et al., 2013). In contrast to the temperature, the normalized amplitude of Ps conversions (Figure 2(e), median -0.88 (Agius et al., 2017)) displays a more diffuse spatial pattern. Indeed, the halo is much less distinctive in the map of the inferred shear wave speed, V_S^{inf} (Figure 2(f)). If variations in seismic properties were purely due to thermal effects, V_S^{ref} and V_S^{inf} should be the same within the limit of uncertainties. The difference between these two wave speed distributions, observed at this resolution for the first time, highlights the separation between the thermal and melting anomalies.

Our analysis shows that the patches which contain the highest melt fractions lie outside the hot plume stem. The residual anomaly, ΔV_S, (Figure 3(a)) is mostly negative (median value of $-1.8\pm0.9\%$) within the LVL, implying the presence of partial melt. The melt distribution (median value of 0.4 $\pm$ 0.3%) closely follows the distribution of ΔV_S, as illustrated in Figure 3(b). Parts of the LVL containing melt-volume fractions that exceed 1 vol% are associated with the region between the plume stem and the halo (indicated by isotherms in Figure 3(b)). In turn, the melt volume fraction is $\leq$0.5 vol% within the plume stem (and even lower within the cold halo). This observation contradicts the expected spatial association between regions of high melt volume fraction with regions of high temperatures, suggesting instead, that the melt must have been carried away from the plume stem. The fact that this melt displacement must be associated with mantle flow, is demonstrated by a calculation of melt permeability and related buoyancy-driven melt-solid segregation velocities (Figure s 3(c) and (d)). The relatively low inferred permeabilities ($\sim 10^{-14}\text{m}^2$) and melt-segregation velocities ($\sim$20 μm/yr) suggest that the $\sim$0.4 vol% melt in and near the plume stem are practically immobile relative to the matrix, implying an important horizontal flow component of the matrix.

3.2. The effect of Clapeyron slope, solid composition, and dihedral angle

Figure 4(a) shows the histogram for the calculated thermal anomalies for three different values of the Clapeyron slope of olivine-wadsleyite transition. An increase in the Clapeyron slope from 2 MPa/K to 4 MPa/K, leads to a tighter probability distribution function centered around $\Delta T = 0$, with no visible shift of the median value of the distribution. The maps in panels (b) and (d) of Figure 4 show the calculated temperature anomaly distribution for two different values of the Clapeyron slope. The primary influence of the parameter Clapeyron slope is on the spread of the calculated thermal anomaly. In turn, the median of inferred melt volumes remains virtually unaffected by variations in Clapeyron slope (Figure 4(c)), since the central tendency of the probability distribution in panel (a) is insensitive to the variations in the Clapeyron slope.

In addition to the Clapeyron slope of the olivine-to-wadsleyite phase transition, we also explore the effects of the solid-melt dihedral angle for different basalt fractions in the solid (Figure 5(a)). At higher dihedral angles, more melt is confined to grain corners, resulting in a smaller fraction of wetted grain boundaries. This leads to more effective intergranular contacts and stronger skeletal networks of grains. To explain the calculated wave speed anomalies, therefore, a larger melt volume fraction is required (Hier-Majumder, 2008; Hier-Majumder and Abbott, 2010). But similar to the effects of recycled slab component, discussed next, this trade-off does not change our main conclusions.

Following the analysis of single crystals in Hawaiian lavas, Sobolev et al. (2007, 2005) estimated that the Hawaiian plume source contains approximately 20% recycled slab component in addition to pyrolite. This basaltic component may be filtered near the top of the MTZ due to mechanical sequestration into a deep eclogitic pool (Ballmer et al., 2013; Cheng et al., 2015). Such a sequestration is promoted by a maximum of the negative density anomaly of (silica-normative) basaltic materials in the depth range of about 300-410 km depth (Aoki and Takahashi, 2004). The mechanical sequestration of basalt-rich matrix into the deep eclogitic pool occurs by lateral spreading of this neutrally buoyant matrix just beneath the depth of density inversion (Ballmer et al., 2013). The extent of the related segregation of basalt from the rest of the mantle, however, remains poorly constrained. While the lower limit of eclogite fraction f in the LVL is 20% (*i.e.* no segregation), the upper limit may be much higher. In this work, we report results for $f = 27\%$, i.e. near the lower bound.

Here, we quantify the effect of variable basalt fraction in the solid on the calculated melt-volume fractions (Figure 5, also see Figure 4(c)). We find that the reference wave speed increases with increasing f, well explained by the higher elastic moduli of eclogite compared to pyrolite. Accordingly, more melt is required for higher f in order to explain the observed residual shear wave speed anomalies. In turn, smaller basalt contents yield smaller inferred melt fractions. Nevertheless, finite melt fractions in the LVL of a similar order of magnitude are always required for $f \geq 20\%$. Thus, our main conclusions remain robust independent of f. As shown in Figure 5, the same statement is true for the combined effects of f and solid-melt dihedral angle.

The maps in Figure 5(c) depict the distribution of melt vol% for four different volume fractions of f. As shown in the maps, with increasing f, the calculated melt volume fractions show an overall increase, but the pattern of melt distribution remains virtually unaffected. The most melt-rich region occurs to the east of the hot plume stem, near the 1580°C isotherm. Note that any finite melt fractions imply significant volatile fluxes to the LVL, due to the strongly incompatible behavior of H_2O and CO_2 (Aubaud, 2004; Hirschmann and Dasgupta, 2009).

3.3. The relationship between temperature and LVL thickness

An important outcome of our analysis is that the thickness and internal structure of the LVL is clearly distinct from the temperature field inferred from MTZ thickness. As shown in Figure 6(a), there is no visible correlation between LVL thickness and temperature. In Figure 6(b), we plot the unprocessed amplitude of Ps conversion as a function of the calculated melt fractions. As the color of the symbols indicate, for a given measured amplitude, variations in melt fraction arise from variations in temperature, as their effects trade-off with each other. Once the effects of temperature are corrected for by subtracting the reference wave speed V_S^{ref}, the residual anomaly only depends on melt fraction (Figure 6(d)). The color of the points in Figure 6(c) show that higher melt fractions, up to 1.7 vol%, are associated with larger negative ΔV_S. Ultimately, the residual ΔV_S and the inferred melt fractions are not strongly controlled by temperature (*i.e.*, no correlation), consistent with our interpretation of volatile-assisted melting.

3.4. Results from temperature calculations using 410 km topography

The maps in Figure 7 show the results of our inversion for melt content using the topography of the 410-km discontinuity to determine temperature, *i.e.* instead of MTZ topography. These calculations were carried out for a potential temperature of 1427°C, bulk excess eclogite fraction of 27%, a dihedral angle of 25°, and a Clapeyron slope of olivine to wadsleyite transition of 3 MPa/K. The median melt volume fraction for this calculation is 0.3 vol%, similar to that obtained by using the MTZ thickness as a proxy for temperature. As the maps indicate, the plume stem appears wider and the cold 'halo' is substantially reduced in this approach compared to that shown in Figure 2. As shown by the work of Tauzin and Ricard (2014), crustal effects above plumes can lead to overestimation of 410 km depth and introduce errors in the inferred temperature. Using the thickness of MTZ as a proxy eliminates this source of error. While we prefer the temperatures that are calculated from MTZ thickness, some earlier publications used 410-km topography as a proxy for temperature. Thus, we include this result for reference here.

4. Volatile fluxes from the leaky plume

The separation between thermal and chemical signatures provides us with an indication of the geodynamic processes operative within the Hawaiian LVL. Based on our seismic observations and calculated melt volume fractions, two distinct patterns of flow within the LVL can be discerned when the map of temperature in Figure 2(c) is compared with the map of melt distribution in 3(b) (also the cartoon in 8(a)). Dominantly vertical up and downwelling flows, driven by thermal buoyancy, are consistent with the inferred thermal structure in Figure 2(c). In turn, practically immobile melt fractions—evidenced by an average melt percolation speed of 22 μm/yr within and near the plume conduit (Figure 3(d))—indicate a second, dominantly horizontal flow of the plume matrix. Such spreading and stagnation of a "thermochemical" plume, which contains a significant fraction of basaltic material in addition to peridotite (Sobolev et al., 2007), can be caused by a sharp decrease of the buoyancy of basaltic material just above 410 km depth (Aoki and Takahashi, 2004; Ballmer et al., 2013). Spreading and pooling of eclogitic material at the periphery of the Hawaiian plume at these depths is consistent with a regional joint-seismic tomography model(Cheng et al., 2015), as well as with a recent receiver-function study (Kemp et al., 2019), and provides a mechanism for the long-term stabilization of melts away from the plume stem. As the incipient melt is dragged away from the hot plume stem, it does not freeze, because the pooling eclogitic material remains warm (Ballmer et al., 2013), and hence well above the volatile-rich solidi (Figure 8(b)). The leaked melt slowly accumulates outside the plume stem over time, explaining the observed higher melt content in comparison to the plume stem. We can use the seismic observation to further constrain the origin of this melt. Comparison between the carbonated basalt (Thomson et al., 2016) and hydrous peridotite (Ohtani et al., 2004) solidi and our inferred temperatures (*i.e.*, 1440-1640°C; Figure 8(b)) illustrates that the observed melts must be generated by volatiles in the plume. It is important to notice that our melt fraction calculations were not constrained by any solidus, the coincidence of the seismically derived temperature and pressure and the solidi is thus completely independent of the rock physics analysis.

The leakage of melt from the Hawaiian plume leads to a substantial volatile flux back into the mantle. These lost volatiles may never reach the uppermost mantle, or even the atmosphere. Due to the strongly incompatible nature of H_2O (Aubaud, 2004) and CO_2 (Hirschmann and Dasgupta, 2009), the observed 0.4 vol% partial melt can store 3.7 wt% H_2O and 5.5 wt% CO_2 (see Appendix A), substantially higher than the measured concentrations of these volatiles in olivine-hosted melt inclusions from Hawaiian lavas (Hauri, 2002). Using our observed LVL thicknesses and melt-volume fractions, as well as published partition coefficients and volatile abundances in the plume source, we estimate that the Hawaiian plume can leak between 0.7 and 10.7 Mt/yr of CO_2 and between 0.6 and 1.9 Mt/yr of H_2O to the LVL. For comparison, the present day CO_2 surface flux at the Kilauea volcano is measured at 2.4 Mt/yr (Burton et al., 2013). Given the observed global correlations between plumes and LVLs (Vinnik and Farra, 2007), and this estimated loss to the LVL, the global CO_2 flux carried by plumes—before they enter the MTZ—needs to be significantly higher than the estimated 4–110 Mt/yr of CO_2 outgassed at hotspots (Dasgupta and Hirschmann, 2010). Similarly, significant amounts of H_2O carried by mantle upwellings may never reach the surface. These estimated fluxes demonstrate that LVLs act as gatekeepers for mantle volatiles, but are currently neglected in models of global volatile cycles (Dasgupta and Hirschmann, 2010; Kelemen and Manning, 2015; Plank and Manning, 2019). Additionally, the higher incompatibility of CO_2 relative to H_2O (Aubaud, 2004; Hirschmann and Dasgupta, 2009), coupled with the small degree of melting, will tend to preferentially sequester the former into the LVL and back into the deep mantle (Hirschmann and Dasgupta, 2009). Such carbon enrichment of the LVL and deep mantle, a reservoir that has previously not been accounted for, can explain some or all of the missing mantle carbon, reconciling the seemingly discrepant observation of lower C:H ratio in the known mantle reservoirs compared to chondritic meteorites (Hirschmann and Dasgupta, 2009). Further constraints on the global leakage of volatiles at mantle plumes may advance our understanding of volatile delivery to Earth, and across the early solar system.

5. Conclusions

In this study, our rock physics analysis of teleseismic P-to-S conversions reveal the internal structure and melt distribution of the LVL above the Hawaiian MTZ. Our key conclusions are:

- The Hawaiian LVL is characterized by patches containing up to 1.7 vol% melt outside the hot plume stem, while the regional melt distribution has a median of 0.4±0.3 vol%.
- The small melt volume fraction in the LVL, owing to reduced permeability, leads to a median melt segregation velocity of ~ 20 μm/year, effectively trapping the melt within the matrix.
- The location of high melt concentration, coupled with low melt mobility, suggests a possible lateral transport or leakage of matrix-trapped melt, away from the plume stem.

- Based on published petrological and geochemical data, we infer that the Hawiian plume can leak up to 1.9 Mt/yr H_2O and 10.7 Mt/yr CO_2 to the LVL.

Acknowledgment

C.A.R. and N.H. acknowledge funding from the Natural Environment Research Council (NE/M003507/1 and NE/K010654/1) and the European Research Council (GA 638665). SH-M acknowledges support from National Science Foundation, USA (EAR 1215800). The inversions on MuMaP were carried out on ARCHER.

Appendix A. Calculation of volatile fluxes

Based on our calculation of melt-migration velocities, which remain very small, we infer that the volatiles are carried away from the plume stem via immobile melt trapped in the triple grain junctions, i.e. by a laterally-spreading flow of the mantle matrix rather than melt percolation through the matrix. In this section, we present a zeroth order calculation of the flux of volatiles associated with the lateral spreading. Our calculations make a few simplifying assumptions, such as uniform leakage of melt around the plume stem and volatile concentration within the plume stem is equal to the source concentration. While a detailed model of volatile leakage—capturing these complexities of the flow—is outside the scope of this article, the magnitude of volatile fluxes calculated by this simple approach highlights the importance of this flux, currently ignored in global carbon cycle models.

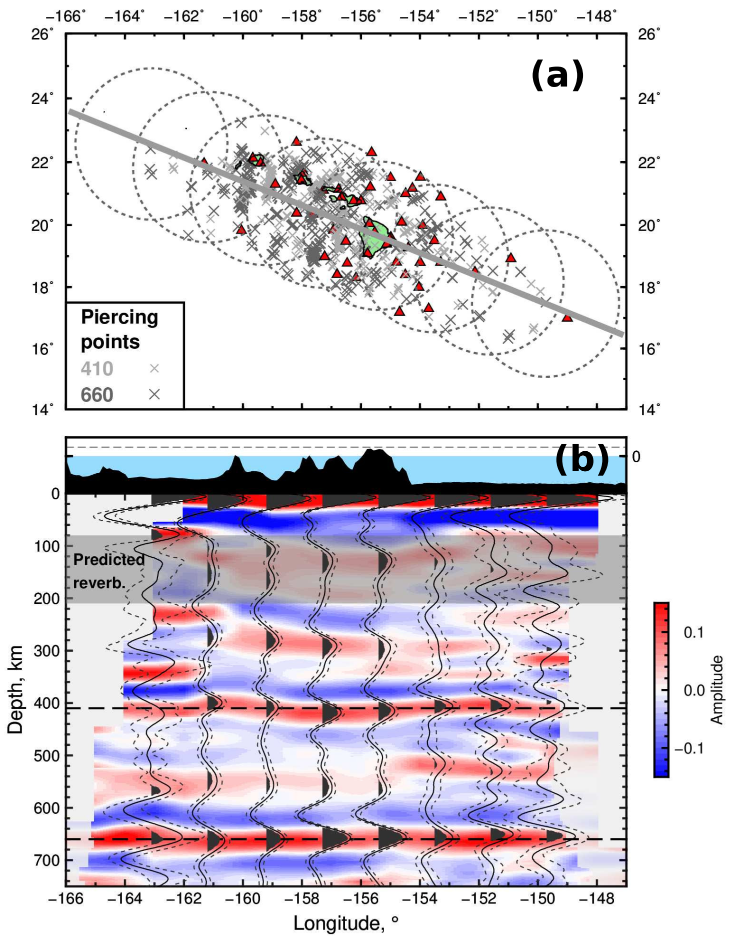

Figure 1: (a) The gray line across the map shows the location of the vertical cross section shown in the panel below. Red triangles are the seismic stations used for the bootstrap. Crosses are the corresponding piercing points at 410- and 660-km depth. (b)Vertical cross-sections through the 3-D depth migrated receiver functions calculated using a crust-corrected PREM wave speed model (Dziewonski and Anderson, 1981). Red and blue shades represent positive and negative amplitudes saturated at ±0.15, respectively. The image resolution is from a 1° by 1° latitude-longitude grid. Semi-transparent shades represent poorly constrained areas due to a low number of traces (<5). Black solid wiggles represent the stacked bin average for the respective area shown on the map above (dashed circles). Dashed wiggles are two standard deviations estimated from bootstrap analysis using 100 randomly selected subsets from within the respective bins. Gray shaded band indicates predicted crustal reverberations.

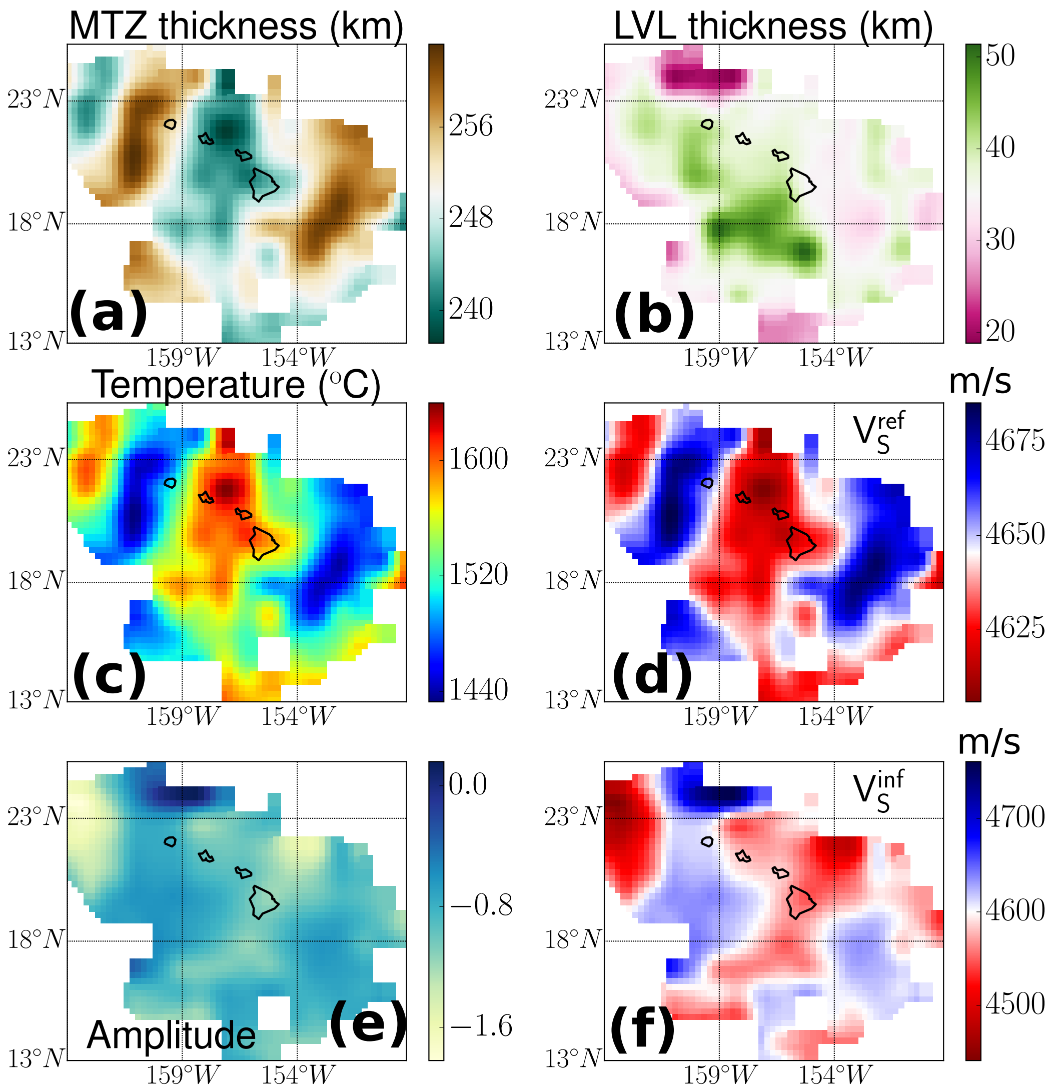

Figure 2: Map of the thermochemical anomalies above the transition zone. (a) Transition zone thickness measured from the Ps conversions. (b) Thickness of the LVL, measured by the distance between the LVL and the top of the MTZ using receiver functions (Agius et al., 2017). (c) The temperature at each point is calculated from the observed transition zone thickness for a mantle potential temperature of 1700 K and a Clapeyron slope for Olivine-Wadsleyite transition of 3 MPa/K. (d) Reference mantle wave speed calculated from the temperature at each point for a mantle eclogite fraction of 27%. (e) The observed amplitude of Ps conversion at the LVL normalized by the amplitude change atop the 410 km discontinuity. (f) The magnitude of shear wave speed calculated from the observed amplitude. (Hier-Majumder et al., 2014).

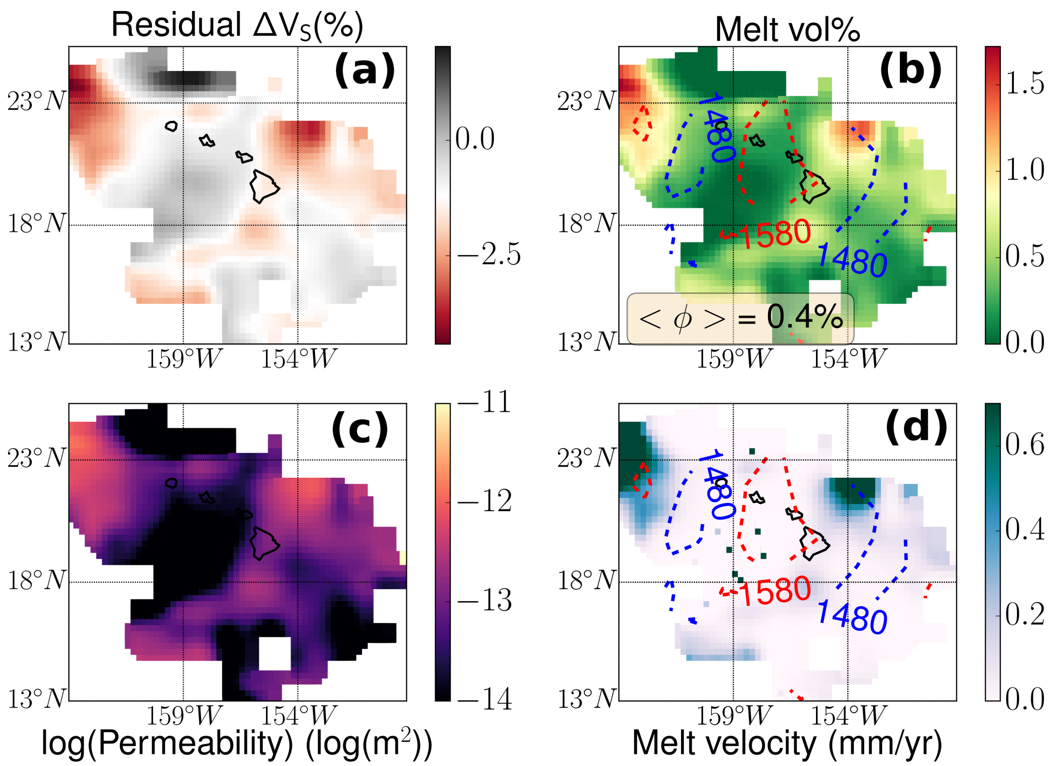

Figure 3: Melt distribution and flow, inferred from the normalized residual wave speed anomaly ΔV_S. (a) Map of ΔV_S, as calculated from V_S^{ref} and V_S^{inf}. (b) Map of melt volume fraction, as calculated from ΔV_S, using a dihedral angle of 25° at the melt grain interface. (c) Map of melt permeability, as calculated from the melt volume fraction at each point using a model of melt tubules along triple grain junctions. The median value of the permeability is 6.0×10^{-14} m^2 (d) Buoyancy-driven segregation velocity of melt in a 1D compacting column, as calculated from an analytical solution of the compaction equations (Hier-Majumder and Courtier, 2011). The median value of the velocity is 22 μm/yr.

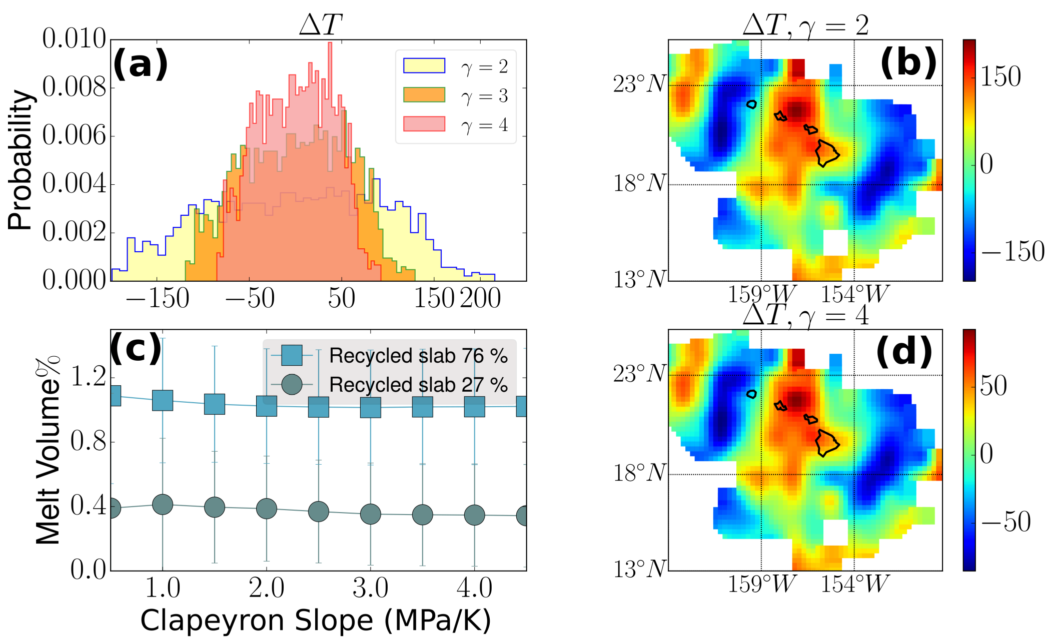

Figure 4: (a) Histogram showing the probability distribution of calculated temperature anomalies for three different values of Clapeyron slope (γ) of the olivine-wadsleyite transition. Maps of the temperature anomalies for (b) $\gamma = 2$ and (c) $\gamma = 4$. In Figure 4(c), the potential temperature has a constant value of 1700 K. (d) Plot of calculated median melt volume fraction as a function of the Clapeyron slope γ, used to calculate the temperature. Two series of data plots are shown for two different basalt fractions in the bulk composition.

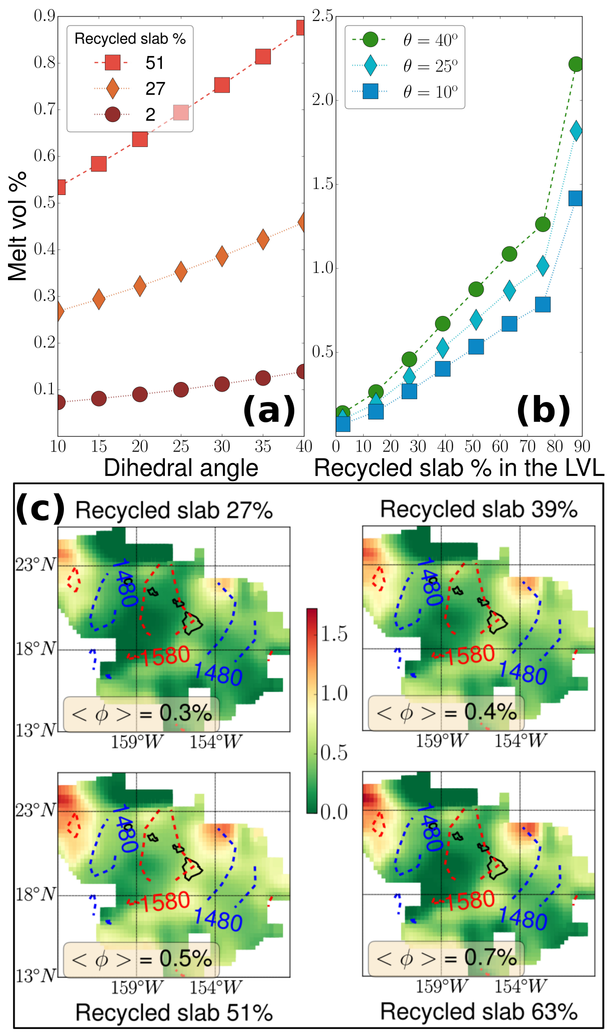

Figure 5: Plot of calculated median melt volume fraction as a function of (a) dihedral angle (θ) (b) and bulk composition (fraction of recycled slab in the mantle, f). (c) Maps of melt volume % for four different values of f. Potential temperature is 1700 K and the dihedral angle is 25^o. The value of median melt vol%, $< \phi >$ for each map is shown in the inset.

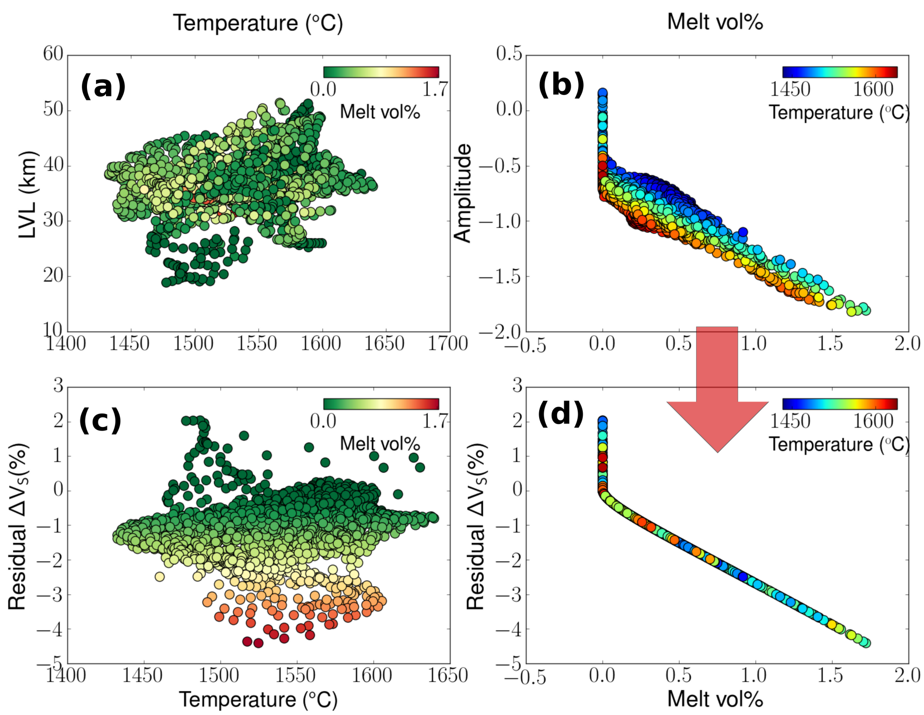

Figure 6: (a) Scatter plot of LVL thickness as a function of the calculated temperature for all data points in this study. The data points are colored by the melt volume fraction calculated at each location. (b) Plot of normalized P-S conversion amplitude as a function of calculated melt volume% at each location in the region. The data points are colored by the temperature at each location. (c) Scatter plot of temperature and the residual shear wave speed ΔV_S. The data points are colored by the melt volume fraction. (d) The residual wave speed anomaly as a function of calculated melt volume%. The data points are colored by the temperature at each location. Spread in the observed amplitude is removed by the thermal correction indicated by the arrow between panels (b) and (d).

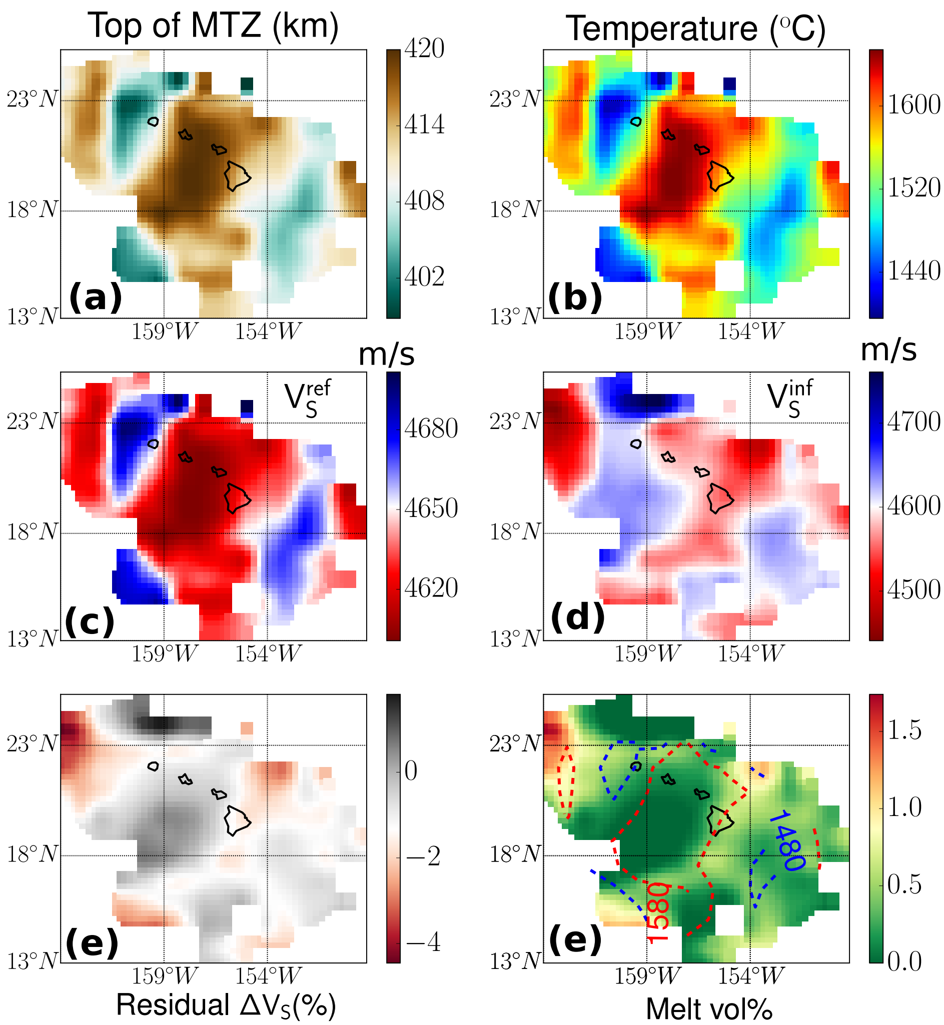

Figure 7: Map of analysis results using the 410 km topography (top of MTZ) to calculate the temperature. (a) Top of the MTZ shown in km. (b) Temperature calculated from the 410 km topography, (c) reference wave speed, (d) inferred wave speed, (e) residual ΔV_s and (f) map of the calculated melt volume% with two isotherms overlain. For these maps, the other parameters are identical to that in Figure s 1 and 2 of the main article.

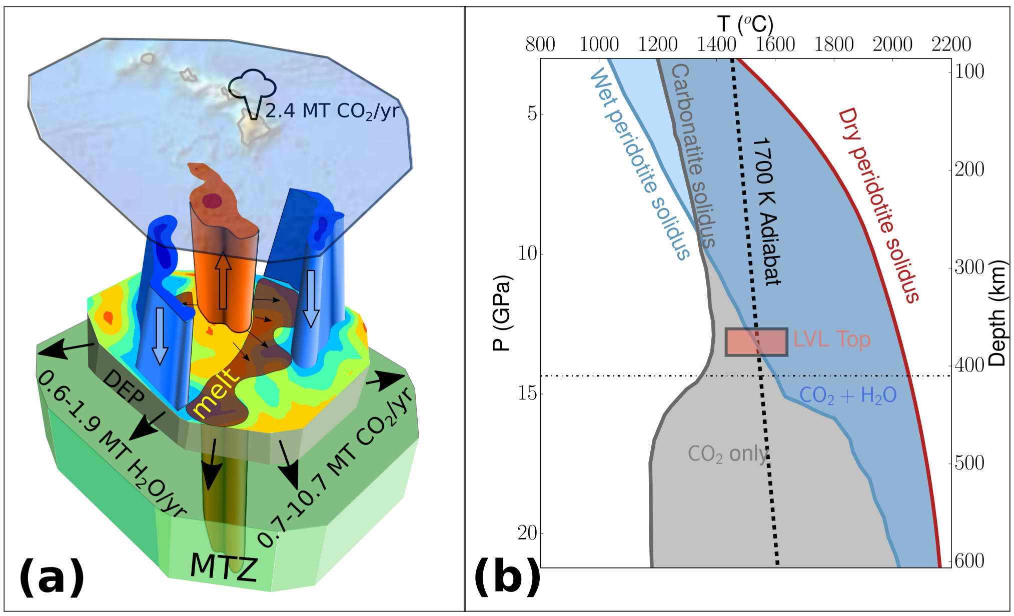

Figure 8: Mantle motion, volatile fluxes, and melting curves for the Hawaiian LVL. (a) A schematic diagram outlining melt leakage around the plume stem aided by lateral flow of a stagnated, spreading deep eclogite pool (DEP) atop the MTZ. The melt-rich regions are shaded in dark brownish red. (b) Solidi of carbonatite (Thomson et al., 2016) and hydrous peridotite (Ohtani et al., 2004) compared with the 1700 K adiabat. Width of the horizontal box corresponds to the range of temperature inferred from the transition zone thickness for the same adiabat. The vertical extent of the box depicts the range of LVL thicknesses inferred in this study.

With the caveat mentioned above, we derive the simple equation to calculate the volatile flux. Assuming a horizontal mantle flow velocity of v, and an LVL thickness of h, the total volume flow per unit time across the vertical boundary of a cylindrical plume stem is given by $2\pi rhv$, where r is the radius of the plume. If the melt volume fraction is given by ϕ, and the melt density by ρ_m, then the melt flow per unit time is $2\pi rhv\phi\rho_m$. Finally, for a volatile concentration of c in the melt, the mass flow rate of the volatile is given by, $2\pi rhv\phi\rho_m c$.

While we do not have a direct way of measuring the concentration of volatiles in the melt, we can use the estimates of the volatile concentration near the center of the plume stem. If this source concentration is given as c_0, and the partition coefficient of the volatile is given by $D^{solid/melt}$, then using the batch melting model, we get,

$$c = \frac{c_0}{(1-D)\phi + D}. \tag{A.1}$$

Using published values of $D^{solid/melt}$, we can calculate the concentration of CO_2 and H_2O in the LVL. For example, for $D_C^{solid/melt} = 0.001$ (Hirschmann and Dasgupta, 2009), $D_H^{solid/melt} = 0.009$ (Aubaud, 2004), source concentrations of $CO_2 = 250$ ppm (Anderson and Poland, 2017) and $H_2O = 450$ ppm (Bizimis and Peslier, 2015), and our median melt volume fraction of 0.0035, we get 5.5 wt% CO_2 and 3.7 wt% H_2O in the LVL. Next, we can use this formula to calculate the fluxes of each of these volatiles away from the plume,

$$F = 2\pi rhv\phi\rho_m \left[\frac{c_0}{(1-D)\phi + D}\right]. \tag{A.2}$$

We use the median values of LVL thickness, $h = 35$ km, and melt volume fraction, $\phi = 0.0035$, from this study, $\rho_m = 3400\mathrm{kg/m^3}$ (Ghosh et al., 2007),

$v = 10$ cm/yr (Ballmer et al., 2013), and $r = 100$ km. To estimate the upper and lower bounds of CO_2 and H_2O fluxes, we use the estimates of c_0 =120-1830 ppm CO_2 and c_0 =300-900 ppm H_2O in the OIB source (Hirschmann and Dasgupta, 2009). These values lead to the flux ranges of 0.7 to 10.7 Mt/yr of CO_2 and 0.6 to 1.9 Mt/yr of H_2O, respectively.

References

Agius, M. R., Rychert, C. A., Harmon, N., Laske, G., 2017. Mapping the mantle transition zone beneath Hawaii from Ps receiver functions : Evidence for a hot plume and cold mantle downwellings. Earth and Planetary Science Letters 474, 226–236.

Anderson, K. R., Poland, M. P., 2017. Abundant carbon in the mantle beneath Hawai'i. Nature Geoscience 10 (9), 704–708.

Aoki, I., Takahashi, E., 2004. Density of MORB eclogite in the upper mantle. Physics of the Earth and Planetary Interiors 143 (1-2), 129–143.

Aubaud, C., 2004. Hydrogen partition coefficients between nominally anhydrous minerals and basaltic melts. Geophysical Research Letters 31 (20), 2–5.

Ballmer, M. D., Ito, G., Wolfe, C. J., Solomon, S. C., 2013. Double layering of a thermochemichal plume in the upper mantle beneath Hawaii. Earth Planet. Sci. Lett. 376, 155–164.

Bell, S. W., Forsyth, D. W., Ruan, Y., 2015. Removing noise from the vertical component records of ocean-bottom seismometers: Results from year one of the cascadia initiative. Bulletin of the Seismological Society of America 105 (1), 300–313.

Bercovici, D., Karato, S., 2003. Whole-mantle convection and the transition zone water filter. Nature 425, 39–44.

Bercovici, D., Ricard, Y., Schubert, G., 2001. A two-phase model for compaction and damage; 1, General theory. Journal of Geophysical Research, B, Solid Earth and Planets 106 (5), 8887–8906.

Bizimis, M., Peslier, A. H., 2015. Water in Hawaiian garnet pyroxenites: Implications for water heterogeneity in the mantle. Chemical Geology 397, 61–75.

Burton, M. R., Sawyer, G. M., Granieri, D., 2013. Deep Carbon Emissions from Volcanoes. Reviews in Mineralogy and Geochemistry 75 (1), 323–354.

Cheng, C., Allen, R. M., Porritt, R. W., Ballmer, M. D., 2015. Seismic Constraints on a Double-Layered Asymmetric Whole-Mantle Plume Beneath Hawai'i. In: Carey, R and Cayol, V and Poland, M and Weis, D (Ed.), HAWAIIAN VOLCANOES: FROM SOURCE TO SURFACE. Vol. 208 of Geophysical Monograph Book Series. Amer Geophys Union, pp. 19–34.

Crawford, W. C., Webb, S. C., 2000. Identifying and Removing TiltNoise from Low Frequency LT0.1Hz Seafloor Vertical Seismic Data. Bulletin of the Seismological Society of America 90 (4), 952–963.

Dasgupta, R., Hirschmann, M. M., 2010. The deep carbon cycle and melting in Earth's interior. Earth Planet Sci. Lett 298, 1–13.

Deuss, A. ., 2009. Global observations of mantle discontinuities using ss and pp precursors. Surv. Geophys. 30, 301–32.

Dziewonski, A. M., Anderson, D. L., 1981. Preliminary reference Earth model. Physics of the Earth and Planetary Interiors 25 (4), 297–356.

Ghosh, S., Ohtani, E., Litasov, K., Suzuki, A., Sakamaki, T., NOV 22 2007. Stability of carbonated magmas at the base of the Earth's upper mantle. GEOPHYSICAL RESEARCH LETTERS 34 (22).

Hauri, E., 2002. SIMS analysis of volatiles in silicate glasses, 2: Isotopes and abundances in Hawaiian melt inclusions. Chemical Geology 183 (1-4), 115–141.

Hier-Majumder, S., DEC 11 2008. Influence of contiguity on seismic velocities of partially molten aggregates. Journal of Geophysical Research-Solid Earth 113 (B12), B12205.

Hier-Majumder, S., Feb. 2020. sashgeophysics/mumap: Mumap v2.1.
URL `https://doi.org/10.5281/zenodo.3673226`

Hier-Majumder, S., Abbott, M. E., OCT 15 2010. Influence of dihedral angle on the seismic velocities in partially molten rocks. Earth and Planetary Science Letters 299 (1-2), 23–32.

Hier-Majumder, S., Ballmer, M., Agius, M., Rychert, C., Harmon, N., 7 2019. Hawaii LVL rock physics inversion data.
URL https://royalholloway.figshare.com/articles/dataset/Hawaii$_{L}VL_{r}ock_{p}hysics_{i}nve$

Hier-Majumder, S., Courtier, A., 2011. Seismic signature of small melt fraction atop the transition zone. Earth and Planetary Science Letters 308 (3-4), 334–342.

Hier-Majumder, S., Keel, E., Courtier, A., 2014. The influence of temperature, bulk composition, and melting on the seismic signature of the low velocity layer above the transition zone. J. of Geophys. Res. Solid Earth 119.

Hier-Majumder, S., Ricard, Y., Bercovici, D., AUG 30 2006. Role of grain boundaries in magma migration and storage. Earth and Planetary Science Letters 248 (3-4), 735–749.

Hier-majumder, S., Tauzin, B., 2017. Pervasive upper mantle melting beneath the western US. Earth and Planetary Science Letters 463, 25–35.

Hirschmann, M. M., Dasgupta, R., May 2009. The H/C ratios of Earth's near-surface and deep reservoirs, and consequences for deep Earth volatile cycles. Chemical Geology 262 (1-2), 4–16.

Kelemen, P. B., Manning, C. E., 2015. Reevaluating carbon fluxes in subduction zones, what goes down, mostly comes up. Proceedings of the National Academy of Sciences 112 (30), E3997–E4006.

Kemp, M., Jenkins, J., Maclennan, J., Cottaar, S., 2019. X-discontinuity and transition zone structure beneath hawaii suggests a heterogeneous plume. Earth and Planetary Science Letters 527, 115781.

Kohlstedt, D., Keppler, H., Rubie, D., 1996. Solubility of water in the α, β and γ phases of $(\mathrm{Mg,Fe})_2\mathrm{SiO}_4$. Contributions to Mineralogy and Petrology 123, 345–357.

Laske, G., Collins, J. A., Wolfe, C., Solomon, S., Detrick, R.S.and Orcutt, J. B. D., Hauri, E., 2009. Probing the hawaiian hot spot with new ocean bottom instruments. EOS, Trans. Am. geophys. Un. 90, 362–3.

Laske, G., Markee, A., Orcutt, J. A., Wolfe, C. J., Collins, J. A., Solomon, S. C., Detrick, R. S., Bercovici, D., Hauri, E. H., 2011. Asymmetric shallow mantle structure beneath the Hawaiian Swell-evidence from Rayleigh waves recorded by the PLUME network. Geophysical Journal International 187 (3), 1725–1742.

Laske, G., Masters, G.and Ma, Z., Pasyanos, M., 2013. Update on crusti.0 - a 1-degree global model of earths crust. p. 2658.

Leahy, G. M., Collins, J. A., Wolfe, C. J., Laske, G., Solomon, S. C., 2010. Underplating of the Hawaiian Swell: Evidence from teleseismic receiver functions. Geophysical Journal International 183 (1), 313–329.

Minarik, W., Watson, E. B., 1995. Interconnectivity of carbonate melt at low melt fraction. Earth Planet Sci. Lett. 133, 423–437.

Ohtani, E., Litasov, K., Tomofumi, H., Kubo, T., Kondo, T., jun 2004. Water transport into the deep mantle and formation of a hydrous transition zone. Physics of The Earth and Planetary Interiors 143-144, 255–269.

Plank, T., Manning, C. E., 2019. Subducting carbon. Nature 574 (7778), 343–352.
URL `http://dx.doi.org/10.1038/s41586-019-1643-z`

Rychert, C. A., Laske, G., Harmon, N., Shearer, P. M., 2013. Seismic imaging of melt in a displaced Hawaiian plume. Nature Geoscience 6 (8), 657–660.

Schulze, K., Marquardt, H., Kawazoe, T., Boffa Ballaran, T., McCammon, C., Koch-Müller, M., Kurnosov, A., Marquardt, K., 2018. Seismically invisible water in Earth's transition zone? Earth and Planetary Science

Letters 498, 9–16.
URL https://doi.org/10.1016/j.epsl.2018.06.021

Shearer, P., 1990. Seismic imaging of upper-mantle structure with new evidence for a 520-km discontinuity. Nature 344, 121–126.

Sobolev, A. V., Hofmann, A. W., Kuzmin, D. V., Yaxley, G. M., Arndt, N. T., Chung, S.-L., Danyushevsky, L. V., Elliott, T., Frey, F. a., Garcia, M. O., Gurenko, A. a., Kamenetsky, V. S., Kerr, A. C., Krivolutskaya, N. a., Matvienkov, V. V., Nikogosian, I. K., Rocholl, A., Sigurdsson, I. a., Sushchevskaya, N. M., Teklay, M., apr 2007. The amount of recycled crust in sources of mantle-derived melts. Science (New York, N.Y.) 316 (5823), 412–7.

Sobolev, A. V., Hofmann, A. W., Sobolev, S. V., Nikogosian, I. K., 2005. An olivine-free mantle source of hawaiian shield basalts. Nature 434 (7033), 590.

Sun, Y., Hier-Majumder, S., Xu, Y., Walter, M., 2020. Stability and migration of slab-derived carbonate-rich melts above the transition zone. Earth and Planetary Science Letters 531, 116000.
URL https://doi.org/10.1016/j.epsl.2019.116000

Tauzin, B., Debayle, E., Wittlinger, G., 2010. Seismic evidence for a global low-velocity layer within the Earth's upper mantle. Nature 3, 718–721, doi:10.1038/NGEO969.

Tauzin, B., Ricard, Y., 2014. Seismically deduced thermodynamics phase diagrams for the mantle transition zone. Earth and Planetary Science Letters 401, 337–346.

Thomson, A. R., Walter, M. J., Kohn, S. C., Brooker, R. A., 2016. Slab melting as a barrier to deep carbon subduction. Nature 1 (2005), 1689–1699.

Turcotte, D., Schubert, G., 2001. Geodynamics. John Willey & Sons.

Vinnik, L., Farra, V., 2007. Low S velocity atop the 410-km discontinuity and mantle plumes. Earth and Planetary Science Letters 262, 398–412, doi:10.1016/j.epsl.2007.07.051.

Wei, S. S., Shearer, P. M., 2017. A sporadic low-velocity layer atop the 410km discontinuity beneath the Pacific Ocean. Journal of Geophysical Research: Solid Earth 122 (7), 5144–5159.

Wimert, J. T., Hier-Majumder, S., 2012. A three-dimensional microgeodynamic model of melt geometry in the earth's deep interior. Journal of Geophysical Research-Solid Earth 117 (B04), B04203.

Wolfe, C. J., Solomon, S. C., Laske, G., Collins, J. a., Detrick, R. S., Orcutt, J. a., Bercovici, D., Hauri, E. H., Dec. 2009. Mantle shear-wave velocity structure beneath the Hawaiian hot spot. Science (New York, N.Y.) 326 (5958), 1388–90.

Wolfe, C. J., Solomon, S. C., Laske, G., Collins, J. a., Detrick, R. S., Orcutt, J. a., Bercovici, D., Hauri, E. H., Mar. 2011. Mantle P-wave velocity structure beneath the Hawaiian hotspot. Earth and Planetary Science Letters 303 (3-4), 267–280.

Xu, W., Lithgow-Bertolini, C., Stixrude, L., Ritsema, J., 2008. The effect of bulk composition and temperature on mantle seismic structure. Earth Planet Sci. Lett. 275, 70–79.